



Two-phase plate-fin heat exchanger modeling for waste heat recovery systems in diesel engines



Emanuel Feru^{a,*}, Bram de Jager^a, Frank Willems^{a,b}, Maarten Steinbuch^a

^a Department of Mechanical Engineering, Eindhoven University of Technology, The Netherlands

^b Powertrain Department, TNO Automotive, The Netherlands

HIGHLIGHTS

- A dynamic model for a modular plate-fin heat exchanger is presented.
- The model combines a finite difference modeling approach with a moving boundary one.
- Multiple phase transitions along a single pipe flow are captured.
- The model is validated on a highly dynamic world harmonized transient cycle.
- The model computational complexity is low, suitable for embedded control purposes.

ARTICLE INFO

Article history:

Received 17 January 2014

Received in revised form 18 July 2014

Accepted 20 July 2014

Available online 12 August 2014

Keywords:

Waste heat recovery

Rankine Cycle

Heat exchanger

Diesel engine

Dynamic model

ABSTRACT

This paper presents the modeling and model validation for a modular two-phase heat exchanger that recovers energy in heavy-duty diesel engines. The model is developed for temperature and vapor quality prediction and for control design of the waste heat recovery system. In the studied waste heat recovery system, energy is recovered from both the exhaust gas recirculation line and the main exhaust line. Due to the similar design of these two heat exchangers, only the exhaust gas recirculation heat exchanger model is presented in this paper. Based on mass and energy conservation principles, the model describes the dynamics of two-phase fluid flow. Compared to other studies, the model is able to capture multiple phase transitions along the fluid flow by combining finite difference approach with moving boundary approaches. The developed model has low computational complexity, which makes it suitable for control design and real-time implementation.

To validate the model, experiments are performed on a state-of-the-art Euro-VI heavy-duty diesel engine equipped with the waste heat recovery system. Simulation results show good accuracy, over the complete engine operating range, with average error below 4%. This is demonstrated on transitions between stationary operating points and on a dynamic response to a standard world harmonized transient cycle for both cold-start and hot-start conditions.

© 2014 Elsevier Ltd. All rights reserved.

1. Introduction

Due to stringent CO₂ emissions regulation, increased fuel costs and concerns about energy security, the automotive industry invests much effort in developing fuel efficient powertrains. Despite that, for trucks the fuel efficiency has been stagnating for the last two decades. However, for CO₂ emissions, USA legislation indicates a 20% reduction by 2020. In Europe, similar requirements are expected to be introduced. Studies [1,2] show that even with

advanced engine technologies around 60–70% of the fuel energy is still lost through the coolant or the exhaust system. Thus, energy recovery from the exhaust is a promising technology allowing a 4–5% increase in the engine efficiency [3–5]. These energy recovery systems are called Waste Heat Recovery (WHR) systems.

The technologies used in a WHR system are various: from mechanical turbo-compounding [6] and electrical turbo-compounding [7] to thermoelectric systems [8] and Rankine Cycles [9]. For heavy-duty applications, the Rankine Cycle promises high potential in terms of costs and overall efficiency improvement of the engine [10]. Moreover, it has been shown in [11] that on a truck diesel engine, due to the low temperature sources, the use of an Organic Rankine Cycle (ORC) appears to be favorable in comparison

* Corresponding author.

E-mail addresses: e.feru@tue.nl (E. Feru), a.g.de.jager@tue.nl (B. de Jager), f.p.t.willems@tue.nl (F. Willems), m.steinbuch@tue.nl (M. Steinbuch).

Nomenclature

A	cross-sectional area, m ²	<i>Subscript and superscript</i>
L	length, m	$*$ dimensionless
M	mass, kg	<i>amb</i> ambient
S	surface area, m ²	<i>avg</i> average
T	temperature, K	c constant
V	volume, m ³	<i>corr</i> correction
\dot{Q}	heat flow rate, W	<i>cs</i> casing
\dot{m}	mass flow rate, kg/s	f working fluid
Nu	Nusselt number, –	g exhaust gas
Pr	Prandtl number, –	h hydraulic
Re	Reynolds number, –	i cell index
c_p	specific heat capacity, J/(kg K)	<i>in</i> inlet
d	diameter, m	<i>ins</i> insulation
e	error, %	l liquid
h	specific enthalpy, J/kg	<i>loss</i> losses
n	number of cells, –	<i>max</i> maximum
p	pressure, Pa	<i>meas</i> measurement
t	time, s	<i>out</i> outlet
x	system state, –	q quality
z	space coordinate, m	r ratio
<i>Greek symbols</i>		s sampling
α	heat transfer coefficient, W/(m ² K)	<i>sat</i> saturation
χ	vapor quality, –	<i>sim</i> simulation
δ	thickness, m	<i>ss</i> steady-state
η	dynamic viscosity, Pa s	v vapor
γ	auxiliary variable, –	<i>vel</i> velocity
λ	thermal conductivity, W/(m K)	w wall
ϕ	system state derivative, –	
ρ	density, kg/m ³	
τ	time constant, s	

with the classical Rankine Cycle. The main difference between the ORC and classical Rankine Cycle is the use of an organic working fluid instead of water [12]. Regardless the Rankine Cycle type, a control design is necessary to optimize the efficiency of the overall WHR system and to ensure safe operation, i.e., no liquid at the heat exchanger outlet. In automotive, control of engines with WHR systems is challenging due to the large number of sensors and actuators, strong coupling between the engine and WHR system and continuous changes in time of the heat available for recovery. Moreover, to maximize the WHR efficiency the system is required to be operated close to the constraint boundaries, while safety is still guaranteed. Thus, dynamical modeling of such systems plays an important role for control and performance prediction.

The dynamic behavior of a WHR system is mainly influenced by the heat exchanger and condenser. These components are most commonly modeled using two approaches: moving boundary models and discretized models. The Moving Boundary (MB) models [13–15] divide the heat exchanger in three regions: liquid, two-phase and vapor separated by boundaries. Due to dynamical conditions, the regions will expand or contract while the position of each phase transition will change. The main idea of MB models is to either track or capture the phase transitions position. However, when the volume of one region becomes much smaller than the others, the MB models become singular [16]. A more robust approach during start-up and shut-down processes is obtained using discretized models, most commonly based on the Finite Volume (FV) [17–19] or Finite Difference (FD) formulation [20,21]. A disadvantage is that discretized models are more computationally expensive due to a larger number of system states.

Many of the heat exchanger models have been designed for large-scale power plants and refrigeration systems. For small-scale

applications characterized by highly dynamic conditions, e.g. automotive applications, only a few studies have been reported. In [22], a dynamic heat exchanger model has been developed and validated for a passenger car application. The model represents a tube-finned heat exchanger based on the MB principle. The studied heat exchanger is non-modular meaning the two flows travel the complete heat exchanger length uniformly. In contrast, we consider a modular heat exchanger design, in which the working fluid side is divided into three sections called modules. These modules are shifted along the heat exchanger length to improve the heat transfer between the flows and to avoid high temperatures in the wall material. In such a design, multiple phase transitions in a single pipe flow can occur, especially during transients. As a result, the modeling of modular heat exchangers using only the MB approach is not straightforward.

In this paper, a dynamic model for a modular plate-fin heat exchanger is presented. The model is developed by combining the FD approach with the MB approach to capture the effect of multiple phase transitions induced by the modular design. The contributions are as follows. First, the mass and energy balance equations for the exhaust gas side, working fluid side, and heat exchanger wall are reconsidered. At the heat exchanger wall, the energy balance includes the transverse conductivity through the wall. To reduce the model complexity a dynamic range analysis is performed. Second, the resulting model is discretized in space and time using a staggered grid approach based on a FD method. Third, to account for the multiple phase transitions, a phase-change detection algorithm is implemented that mimics the MB approach within each discretization cell. Fourth, the model is validated on a state-of-the-art Euro-VI heavy-duty diesel engine equipped with a WHR system. The model validation is performed

over the complete engine operating range and during highly dynamic engine conditions. In comparison with previous developments [23,24], the simulation results demonstrate an improved representation of the real system in terms of accuracy, while the real-time requirements are reached.

The paper is organized as follows. Section 2 presents the layout and working principle of the studied experimental set-up. In Section 3, the mathematical description including the heat transfer relations are given and a non-dimensional form of the heat exchanger model is derived. In Section 4, the resulting partial differential equations are discretized with respect to time and space. The model is experimentally validated and the results are discussed in Section 5. Finally, Section 6 presents the conclusions.

2. System description

The experimental set-up (see Fig. 1) consists of a 375 kW, 12.9 l, 6 cylinder diesel engine, which is equipped with a 2500 bar common rail fuel injection system, a cooled high pressure Exhaust Gas Recirculation (EGR) system, Variable Turbine Geometry (VTG) and Charge Air Cooling (CAC). The exhaust aftertreatment system contains a Diesel Oxidation Catalyst (DOC), a Diesel Particulate Filter (DPF), a Cu–Zeolite SCR catalyst (SCR) and an Ammonia Oxidation catalyst (AMOX) to avoid unwanted NH_3 slip. To meet the upcoming CO_2 regulations, a WHR system is integrated with the engine.

In this WHR system, the heat is recovered from both the EGR line and exhaust line using two evaporators, one for each of the exhaust circuits. The recovered exhaust heat is converted to mechanical power, by means of a piston expander. The piston expander and pumps are mechanically coupled with the engine crankshaft. As a result, the recovered power is directly transmitted to the driveline. The selected working fluid is pure ethanol, because of its physical and thermodynamic properties, which are suitable for applications with low temperature heat sources. The ethanol mass flow is controlled by two bypass valves, one for each evaporator. To close the Rankine Cycle, the ethanol is cooled back before the tank by means of a condenser. To comply with the vehicle and WHR system cooling capabilities, an exhaust bypass valve is installed before the exhaust evaporator. This valve bypasses the exhaust gas and therefore manipulates the input heat for the exhaust evaporator. Due to drivability requirements, the power

delivered by the WHR system must be interrupted temporarily, e.g., during braking or gear shifting. In this case, an electric bypass valve is activated which shuts off the vapor flow to the expander and thereby reduces the generated torque. For safety reasons, a 60 bar pressure relief valve is used that releases the excess vapor flow before the condenser. The electric bypass valve and the pressure relief valve are located in the valve box.

The considered experimental set-up is furthermore equipped with temperature (T), pressure (p) and flow (q) sensors. The measurement system consists of thermocouples of type T and K to measure temperature, thin-film pressure sensors to measure pressure, Coriolis flow meters to measure the exhaust gas mass flow rate and helicoidal flow meters to measure the ethanol mass flow rate. The uncertainty of the measurement due to sensor error is up to 5 K for the temperature, $\pm 1.5\%$ regarding the pressure, and $\pm 0.3\%$ for the exhaust gas and ethanol mass flow rate. These accuracies are indicated by the individual sensor manufacturer. However, when installed in an engine platform, several factors can worsen the measurement accuracy. For instance, the exhaust gas temperature measurement is affected by a non-uniform temperature distribution over the exhaust gas pipe cross section. Furthermore, the fluid mass flow sensor accuracy is given for a constant fluid flow in the pipe. However, in the studied platform the flow is not constant but rather pulsating due to the pumping behavior. These effects influence the accuracy of the measured system performance and of the energy flow rates.

The engine with WHR system is connected to an engine dynamometer for testing the system under any engine load and rotational speed within the engine operating range. Furthermore, the WHR system was protected with insulation material to minimize heat losses to the environment. The layout of the complete system, engine with WHR system, was designed based on the real vehicle layout. The purpose of this set-up is to demonstrate the potential of the WHR system, to develop and validate dynamical models and to design and test control strategies. In this study, recorded data is used to validate a dynamic model for the EGR heat exchanger.

3. Heat exchanger modeling approach

The objective of this study is to develop a heat exchanger model with the following properties: (i) good prediction of the vapor

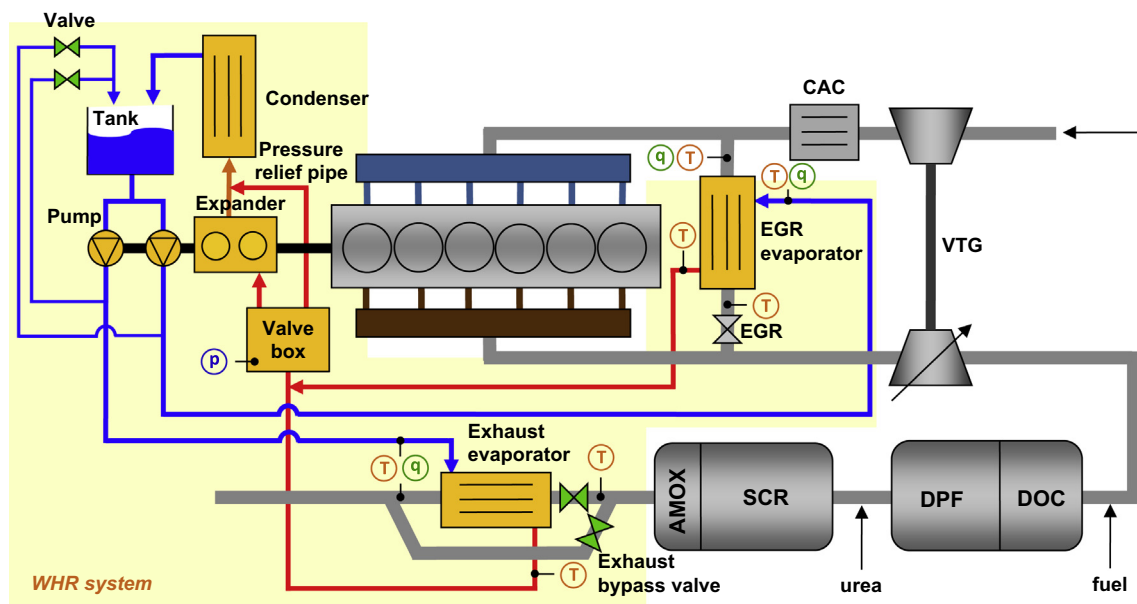


Fig. 1. Schematic representation of a heavy-duty diesel engine equipped with a WHR system.

quality, (ii) good dynamical prediction of the outlet working fluid temperature and (iii) good prediction of the outlet exhaust gas temperature. Each of these properties are proposed for the following reasons: (i) is crucial for safe system operation, (ii) is important for control design and (iii) is in strong relation with the engine out emissions and proper function of the EGR system. In the considered WHR system, two heat exchangers are used that differ in size and geometry. However, the dynamic behavior is similar and can be described by the same mathematical relations. Thus, to avoid repetition, only the EGR evaporator is described.

The EGR evaporator (Fig. 2) is a prototype plate-fin heat exchanger, in which the two fluids flow parallel to each other, but in opposite direction. The plates are vertically aligned and connected with fins. Heat transfer enhancement is achieved by means of a staggered fins arrangement similar to the arrangement in [25].

The heat exchanger is divided into three modules. The main reason for this is to avoid high wall temperatures, which could harm the wall material. In a classical counter-flow heat exchanger design, the wall temperature is highest where the working fluid exits and the exhaust gas enters the heat exchanger. From the working fluid flow direction perspective, by dividing the heat exchanger into three modules and swapping the last two modules the wall peak temperature is reduced. This is due to the fact that a lower exhaust gas temperature corresponds to the module with the working fluid in vapor state. To reduce heat losses to the environment, the heat exchanger is wrapped in an insulation layer.

3.1. Mass and energy conservation

The mathematical description of the heat exchanger is formulated using the general conservation principles for mass and energy. Radiation and viscous friction are neglected, since their contributions are much smaller than the remaining terms. In addition, the exhaust gas change in density is neglected as a function of temperature and pressure, and thus no dynamic mass balance equation is used at the exhaust gas side. Furthermore, we consider the temperature to be uniform along the transverse direction for both the exhaust gas and working fluid. The time derivative of pressure is neglected for both the working fluid side and exhaust gas side. This assumption is made, since the pressure dynamics are considered to be characterized by small time scales in comparison to the relevant thermal phenomena. Thus, no equation for momentum conservation is used. Consequently, the heat exchanger model can be written by the following set of partial differential equations.

Conservation of mass (working fluid):

$$V_f \frac{\partial \rho_f}{\partial t} + L \frac{\partial \dot{m}_f}{\partial z} = 0, \quad (1)$$

Conservation of energy:

$$\rho_g c_{pg} V_g \frac{\partial T_g}{\partial t} = c_{pg} \dot{m}_g L \frac{\partial T_g}{\partial z} - \alpha_g S_g (T_g - T_{wg}) - \dot{Q}_{loss}, \quad (2a)$$

$$\rho_f V_f \frac{\partial h_f}{\partial t} = -\dot{m}_f L \frac{\partial h_f}{\partial z} + \alpha_f S_f (T_{wf} - T_f), \quad (2b)$$

Conservation of energy at the wall:

$$\rho_w c_{pw} \gamma_w V_w \frac{\partial T_{wg}}{\partial t} = \alpha_g S_g (T_g - T_{wg}) - \frac{\lambda_w S_w}{\delta_w} (T_{wg} - T_{wf}), \quad (3a)$$

$$\rho_w c_{pw} (1 - \gamma_w) V_w \frac{\partial T_{wf}}{\partial t} = -\alpha_f S_f (T_{wf} - T_f) + \frac{\lambda_w S_w}{\delta_w} (T_{wg} - T_{wf}), \quad (3b)$$

where L is the heat exchanger length, V_f is the volume occupied by the working fluid including the connecting pipes between modules and V_g is the volume occupied by the exhaust gas. Despite the connecting pipes, for simplicity we assume constant cross sectional area along the heat exchanger length. A constant density ρ_g and heat capacity c_{pg} is assumed for the exhaust gas side. The working fluid density ρ_f however changes as a function of the enthalpy h_f and pressure p_f . For the wall, the volume V_w includes the plate material and fins but not the casing material. Note that a constant factor $\gamma_w = 0.6$ is introduced in (3) to separate the mass of the wall, i.e., $M_w = \rho_w V_w$, including fins on the exhaust side from the mass of the wall on the working fluid side.

Note that in (3) we only consider the transverse wall conduction computed based on two temperature points T_{wg} and T_{wf} . The longitudinal heat conduction is neglected since it is significantly less important than the transverse heat conduction (see, e.g., [13]). This reduces the modeling problem from a two dimensional to a one dimensional problem. Furthermore, the heat conduction between the three heat exchanger modules (Fig. 2) is neglected, since the core (consisting of plates and fins) is separated between modules.

The change in phase occurs only on the working fluid side and not on the exhaust gas side. Therefore, in (2a) we choose to describe the exhaust gas enthalpy using a well known approximation $h_g = c_{pg} T_g$. Furthermore, since the heat exchanger operates within a limited temperature window, a constant heat capacity for the wall c_{pw} is considered. The transverse conductivity in the wall is important for steady-state and dynamic behavior. There are several ways to describe the wall transverse conductivity. For simplicity, in (3) we characterize the wall by two states T_{wg} and T_{wf} , representing the wall surface temperature in contact with the exhaust gas and working fluid, respectively.

The heat loss from an insulated heat exchanger is expressed at steady-state by

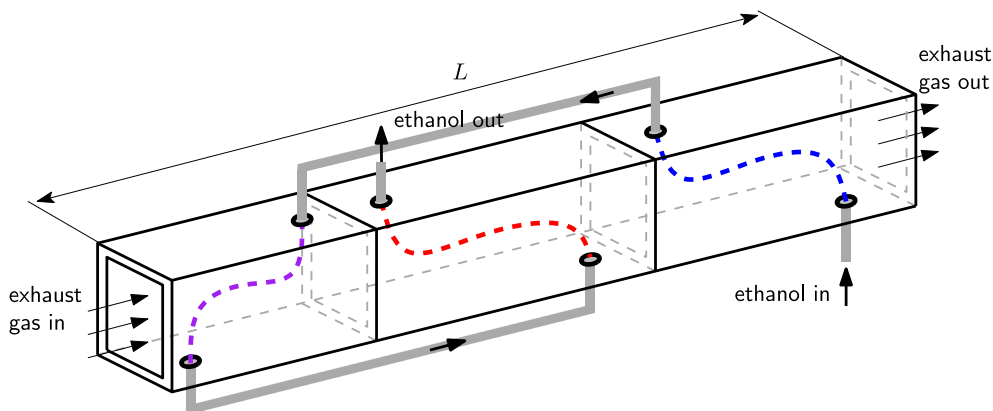


Fig. 2. Diagram of the exhaust gas recirculation heat exchanger modular design.

$$\dot{Q}_{loss,ss} = \frac{S_{cs}(T_{g,avg} - T_{amb})}{\frac{1}{\alpha_g} + \frac{\delta_{cs}}{\lambda_{cs}} + \frac{\delta_{ins}}{\lambda_{ins}} + \frac{1}{\alpha_{amb}}}, \quad (4)$$

where S_{cs} is the heat exchanger casing surface area, δ_{cs} is the thickness and λ_{cs} is the thermal conductivity of the casing, respectively. The insulating layer is characterized by a thickness δ_{ins} and a thermal conductivity λ_{ins} . The average exhaust gas temperature $T_{g,avg}$ is obtained based on the inlet and outlet temperature, i.e., $T_{g,avg} = (T_{g,in} + T_{g,out})/2$. The heat transfer coefficient to the ambient α_{amb} is considered to be constant.

The heating-up thermal inertia of the casing material is introduced as a first order system response:

$$\frac{d\dot{Q}_{loss}}{dt} = \frac{1}{\tau_{cs}} (\dot{Q}_{loss,ss} - \dot{Q}_{loss}), \quad (5)$$

where τ_{cs} is the heat exchanger casing time constant obtained based on the mass and heat capacity of the casing and insulation material.

3.2. Heat transfer

The heat transfer from the exhaust gas to the wall and from wall to the working fluid is modeled as forced convection. In the wall, heat conduction is considered based on the wall conductivity λ_w , the wall thickness δ_w and surface area S_w expressed for one plate.

To describe the convective heat transfer from a moving fluid to the solid boundary (wall), a heat transfer coefficient α is employed. This quantity depends on the relevant fluid and process properties as well as geometrical configurations of the wall. In general, the heat transfer coefficient is determined experimentally and correlations for various technical configurations are derived [26]. For this purpose, a dimensionless heat transfer coefficient called Nusselt number is used:

$$Nu = \frac{\alpha d_h}{\lambda}, \quad (6)$$

where d_h is the hydraulic diameter and λ is the thermal conductivity of the fluid. For parallel plates, the hydraulic diameter d_h is twice the spacing between the plates.

To derive correlations for the Nusselt number in forced convection, two other dimensionless numbers are used, namely the Reynolds number and the Prandtl number. The Reynolds number describes the flow characteristics and is given by:

$$Re = \frac{\dot{m}_{vel} d_h}{\eta}, \quad (7)$$

where \dot{m}_{vel} is the mass velocity and η is the fluid dynamic viscosity. The mass velocity is $\dot{m}_{vel} = \dot{m}/A$ with \dot{m} the mass flow rate and A the flow cross sectional area. Further, the Prandtl number is given by:

$$Pr = \frac{\eta c_p}{\lambda}, \quad (8)$$

where c_p is the heat capacity of the fluid.

On the exhaust gas side, the heat transfer is enhanced by fins and thus, a Nusselt number correlation that can be used for heat transfer coefficient calculation in staggered finned surfaces has to be selected. On the working fluid side, in the liquid region, the Reynolds number indicates the flow is laminar ($Re_l < 2300$) while in the vapor region, the Reynolds number indicates the flow is turbulent ($Re_v > 4000$). Therefore, appropriate Nusselt numbers correlation in single-phase are selected from [26].

Using the appropriate Nusselt numbers correlation for the working fluid, the local single-phase heat transfer coefficients $\alpha_{f,l}$ and $\alpha_{f,v}$ are determined for the liquid and vapor region, respectively. In the two-phase region, the heat transfer coefficient α_f in vertical tubes is used:

$$\frac{\alpha_f}{\alpha_{f,l}} = \left\{ (1 - \chi_q)^{0.01} \left[(1 - \chi_q) + 1.9 \chi_q^{0.6} \left(\frac{\rho_l}{\rho_v} \right)^{0.35} \right]^{-2.2} + \chi_q^{0.01} \left[\frac{\alpha_{f,v}}{\alpha_{f,l}} \left(1 + 8(1 - \chi_q)^{0.7} \left(\frac{\rho_l}{\rho_v} \right)^{0.67} \right) \right]^{-2} \right\}^{-0.5}, \quad (9)$$

where ρ_l and ρ_v are the saturated liquid density and saturated vapor density, respectively. The vapor quality χ_q is obtained from:

$$\chi_q = \max(0, \min(1, \chi_r)), \quad \chi_r = \frac{h_f - h_l}{h_v - h_l}, \quad (10)$$

where χ_r represents the vapor ratio, with h_l and h_v the saturated working fluid enthalpy in liquid state and vapor state at a specific pressure p_f , respectively.

Many empirical correlations for describing the saturated flow boiling exist in the literature [27,28]. The reason for selecting (9) comes from the fact that it covers fluids with values of ρ_l/ρ_v from 3.75 to 1017, i.e., typical for our application. Furthermore, the expression is smooth and goes to its proper limits $\alpha_{f,l}$ and $\alpha_{f,v}$ at $\chi_q = 0$ and $\chi_q = 1$, respectively.

Remark 1. Note that the two-phase heat transfer coefficient (9) corresponds to a tube arrangement. However, the heat exchanger which we aim to model has plates instead of tubes. The main reason for using (9) is that, considering the two-phase nature of our problem, the physics for boiling inside tubes is well-established [26]. Moreover, in Section 5, we will show that using (9) produces a model with acceptable validation properties.

To predict the phase change along the heat exchanger fluid flow, properties of the working fluid have to be provided. In the considered WHR system and experimental set-up, an analysis of the physical and thermodynamic properties indicates that ethanol is a good candidate as a working fluid. In this study, the used working fluid properties are the saturation temperature, the temperature-enthalpy characteristic and the density-enthalpy characteristic. In [23], the ethanol properties have been described mathematically to create independence from chemical databases. Here, a similar approach is used to express the saturation temperature. However, the working fluid temperature, heat transfer coefficient and density as a function of enthalpy changes are smoothed around the liquid and vapor saturated enthalpy h_l and h_v , respectively (see¹ Fig. 3, indicated in red).

The smoothing is performed using cubic functions around an enthalpy range given by Δh . The enthalpy range Δh is a positive value, upper limited by the critical pressure such that the two interpolation cubic functions do not overlap. The first reason of the smoothing is to become more in line with the experiments due to imperfect fluid mixing at the saturation boundaries. The second reason is to avoid discontinuities in the working fluid enthalpy derivative during a phase change, which can lead to chattering phenomena. More details regarding the working fluid properties are given in Appendix A.

3.3. Non-dimensional analysis

In what follows, we bring the system to a non-dimensional form by means of scale analysis. Scale analysis has several advantages: it gives an indication of the important parts of an equation, reduces the number of free parameters while it avoids numerical difficulties.

To non-dimensionalize the system of equations, we first identify the independent and dependent variables. Second, we replace

¹ For interpretation of color in Fig. 3, the reader is referred to the web version of this article.

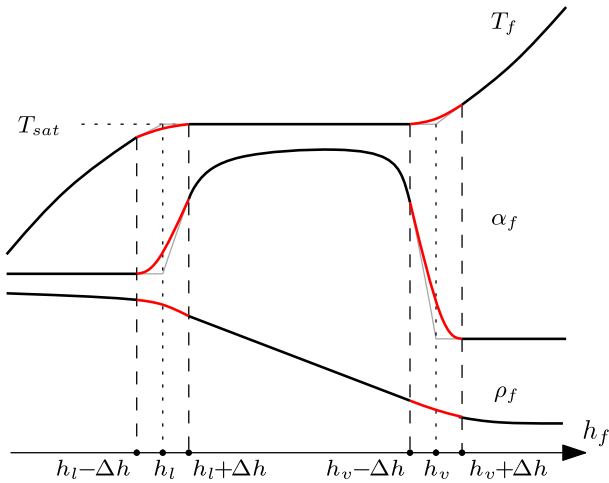


Fig. 3. Smoothed temperature, heat transfer coefficient and density of the working fluid using cubic interpolation functions.

each of them with a quantity scaled relative to a characteristic unit of measure, i.e.,

independent variables : $t^* = \frac{t}{t_{wg}^c}$, $z^* = \frac{z}{L}$;

dependent variables : $h_f^* = \frac{h_f}{h_f^c}$, $h_g^* = \frac{h_g}{h_g^c}$, $T_f^* = \frac{T_f}{T^c}$, $T_g^* = \frac{T_g}{T^c}$,

$$T_{wg}^* = \frac{T_{wg}}{T^c}, \quad T_{wf}^* = \frac{T_{wf}}{T^c}, \quad \dot{m}_f^* = \frac{\dot{m}_f}{\dot{m}_f^c},$$

$$\dot{m}_g^* = \frac{\dot{m}_g}{\dot{m}_g^c}, \quad \rho_f^* = \frac{\rho_f}{\rho_f^c}, \quad \alpha_g^* = \frac{\alpha_g}{\alpha_g^c},$$

$$\alpha_f^* = \frac{\alpha_f}{\alpha_f^c}, \quad \dot{Q}_{loss}^* = \frac{\dot{Q}_{loss}}{\dot{Q}_{loss}^c}.$$

(11)

Next, choose

$$t_g^c = \frac{\rho_g V_g}{\dot{m}_g^c}, \quad t_f^c = \frac{\rho_f V_f}{\dot{m}_f^c}, \quad t_{wg}^c = \frac{\rho_w c_{pw} \gamma_w V_w}{\dot{m}_g^c c_{pg}}, \quad t_{wf}^c = \frac{\rho_w c_{pw} (1 - \gamma_w) V_w T^c}{\dot{m}_f^c h_f^c},$$

$$\alpha_g^c = \frac{\dot{m}_g^c c_{pg}}{S_g}, \quad \alpha_f^c = \frac{\dot{m}_f^c h_f^c}{S_f T^c}, \quad \dot{Q}_{loss}^c = \dot{m}_g c_{pg} T^c.$$

(12)

Then, the mass and energy conservation equations become:

Conservation of mass (working fluid):

$$R_1^* \frac{\partial \rho_f^*}{\partial t^*} + \frac{\partial \dot{m}_f^*}{\partial z^*} = 0, \quad (13)$$

Conservation of energy:

$$R_2^* \frac{\partial T_g^*}{\partial t^*} = \dot{m}_g^* \frac{\partial T_g^*}{\partial z^*} - \alpha_g^* (T_g^* - T_{wg}^*) - \dot{Q}_{loss}^*, \quad (14a)$$

$$\rho_f^* R_1^* \frac{\partial h_f^*}{\partial t^*} = -\dot{m}_f^* \frac{\partial h_f^*}{\partial z^*} + \alpha_f^* (T_{wf}^* - T_f^*), \quad (14b)$$

Conservation of energy at the wall:

$$\frac{\partial T_{wg}^*}{\partial t^*} = \alpha_g^* (T_g^* - T_{wg}^*) - C_1^* (T_{wg}^* - T_{wf}^*), \quad (15a)$$

$$R_3^* \frac{\partial T_{wf}^*}{\partial t^*} = -\alpha_f^* (T_{wf}^* - T_f^*) + C_2^* (T_{wg}^* - T_{wf}^*), \quad (15b)$$

where

Table 1
Heat exchanger time constants.

Parameter	Time (s)	Type
t_{wg}^c	28	Constant
t_{wf}^c	13	Constant
t_g^c	0.3	Constant
t_f^c	[0.2, 8]	Variable

$$R_1^* = \frac{t_f^c}{t_{wg}^c}, \quad R_2^* = \frac{t_g^c}{t_{wg}^c}, \quad R_3^* = \frac{t_{wf}^c}{t_{wg}^c}, \quad C_1^* = \frac{1}{\dot{m}_g^c c_{pg}} \frac{\lambda_w S_w}{\delta_w},$$

$$C_2^* = \frac{T^c}{\dot{m}_f^c h_f^c} \frac{\lambda_w S_w}{\delta_w} \quad (16)$$

In (12), the time constants t_g^c and t_f^c are the residence times. These values are the average amount of time that a particle from the exhaust gas or working fluid travels the complete heat exchanger length. For the wall, t_{wg}^c and t_{wf}^c are the heating-up and cooling-down time constants.

Remark 2. Note that the choice of dimensionless parameters is not unique. A different choice of dimensionless parameters results in a similar system representation that differs only in scale. Here, we have chosen the constants h_f^c , h_g^c , T^c , \dot{m}_f^c , \dot{m}_g^c and ρ_f^c as the maximum values the system can reach inside the operating window.

For this particular heat exchanger, the time constants from (12) are numerically given in Table 1. While t_{wg}^c , t_{wf}^c and t_g^c are constant, t_f^c is variable. The working fluid time constant t_f^c varies due to the change in density along the heat exchanger length. It starts from 8 s in liquid phase and decreases to 0.2 s for the working fluid in vapor phase. The objective is to develop a numerically stable model with low computational complexity that fits typical Electronic Control Units (ECU) specifications. To accomplish this, we neglect the exhaust gas dynamics since t_g^c is significantly small compared to the wall time constant t_{wg}^c . Thus, the energy conservation for the exhaust gas side becomes:

$$0 = \dot{m}_g^* \frac{\partial T_g^*}{\partial z^*} - \alpha_g^* (T_g^* - T_{wg}^*) - \dot{Q}_{loss}^*. \quad (17)$$

To illustrate that this simplification holds, experimental data is used in Section 5. The simplified dynamical behavior of the model is governed by a first order casing model, the working fluid and the wall dynamics. The resulting continuous-time heat exchanger model is given by (5), (13), (14b), (15) and (17).

4. Model discretization

In this section, the continuous-time heat exchanger model is discretized with respect to time and space based on a finite-difference approximation. For the space discretization, a staggered grid is used to calculate the heat flux from the exhaust gas to the wall and from the wall to the working fluid.

First, as shown in Fig. 4, the heat exchanger fluid path is divided into n cells in which the mass conservation principle and energy conservation principle are applied. Note that the parameters (16) are adapted for one cell to incorporate Δz^* , resulting in a more simple expression for (13), (14b), (15) and (17). Thus, the mass balance Eq. (13) for each cell $i = 1, \dots, n$ is given by:

$$\dot{m}_{f,i+1}^* = \dot{m}_{f,i}^* - R_1^* \frac{d\rho_{f,i}^*}{dt}, \quad (18)$$

where $\rho_{f,i}^*$ is the non-dimensional density computed as function of the average enthalpy inside cell i .

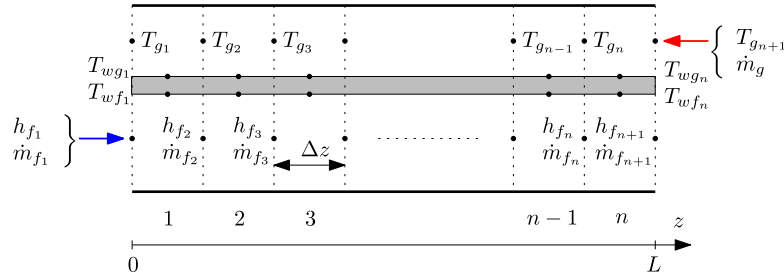


Fig. 4. Staggered space discretization of the heat exchanger length.

Next, let us consider the following dimensionless average values in cell i : $\bar{T}_{g_i}^* = (T_{g_{i+1}}^* + T_{g_i}^*)/2$ for the exhaust gas temperature $\bar{T}_{f_i}^* = (T_{f_{i+1}}^* + T_{f_i}^*)/2$ for the working fluid temperature and $\bar{\alpha}_{f_i}^* = (\alpha_{f_{i+1}}^* + \alpha_{f_i}^*)/2$ for the working fluid heat transfer coefficient. The energy conservation for the exhaust gas (17) has a steady-state form, i.e.,

$$T_{g_i}^* = \frac{(2\dot{m}_g^* - \alpha_g^*)T_{g_{i+1}}^* + 2\alpha_g^*T_{wg_i}^* - 2\dot{Q}_{loss}^*}{2\dot{m}_g^* + \alpha_g^*}. \quad (19)$$

Note that in (19), the exhaust gas temperature profile is computed from right to left corresponding to the flow direction of the fluid.

The conservation of energy for the working fluid and at the wall can be written in discrete-space form as

$$\frac{dh_{f_{i+1}}^*}{dt^*} = \frac{1}{\bar{\rho}_f^* R_1^*} \left(-\dot{m}_{f_i}^* (h_{f_{i+1}}^* - h_{f_i}^*) + \bar{\alpha}_{f_i}^* (T_{wf_i}^* - \bar{T}_{f_i}^*) \right), \quad (20a)$$

$$\frac{dT_{wg_i}^*}{dt^*} = \alpha_g^* (\bar{T}_{g_i}^* - T_{wg_i}^*) - C_1^* (T_{wg_i}^* - T_{wf_i}^*), \quad (20b)$$

$$\frac{dT_{wf_i}^*}{dt^*} = \frac{1}{R_3^*} \left(-\bar{\alpha}_{f_i}^* (\bar{T}_{wf_i}^* - T_{f_i}^*) + C_2^* (T_{wg_i}^* - T_{wf_i}^*) \right). \quad (20c)$$

In (20a), we choose to approximate the working fluid density inside the heat exchanger using $\bar{\rho}_f^* = (1/n) \sum_{i=1}^n \rho_{f_i}^*$.

Second, the continuous-time set of Eq. (20) are discretized in time based on a forward Euler approximation. For simplicity, let us denote:

$$x_i^* = \begin{bmatrix} h_{f_{i+1}}^* \\ T_{wg_i}^* \\ T_{wf_i}^* \end{bmatrix}, \quad \phi_i^*(x_i^*, x_{i-1}^*) = \frac{dx_i^*}{dt^*}, \quad i = 1, \dots, n. \quad (21)$$

Then, the one-step ahead system state $x_i^*(k+1)$ can be approximated using a forward Euler scheme as:

$$x_i^*(k+1) = x_i^*(k) + t_s^* \phi_i^*(x_i^*(k), x_{i-1}^*(k)), \quad i = 1, \dots, n, \quad (22)$$

where t_s^* is a dimensionless sampling rate defined as $t_s^* = t_s/t_{wc}^*$.

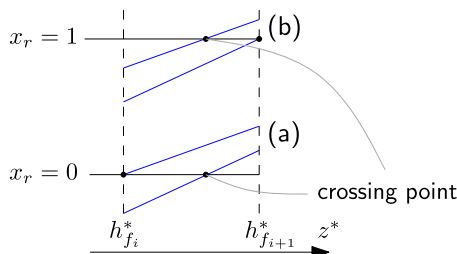


Fig. 5. Representation of two different phase-change detection situations: (a) From liquid to two-phase. (b) From two-phase to vapor.

4.1. Phase-change detection

When modeling two-phase flow heat exchangers, the dynamic information of liquid and vapor region length is of interest for control and heat exchanger performance analysis. However, due to space-discretization of the partial differential Eqs. (13), (14b), (15) and (17), these regions have to be computed algebraically. To address this problem a phase-change detection routine is implemented. As shown in Fig. 5, the phase-change detection finds the crossing point inside a cell i based on the current state information $h_{f_i}^*$ and $h_{f_{i+1}}^*$.

Fig. 5 shows the crossing point detection for a heating-up process. For a cooling-down process a similar approach is employed. As in the MB method also in the phase-change detection routine, the aim is to find the crossing point position (see Fig. 5). However, this becomes more challenging for modular heat exchangers due to multiple phase transitions in a single flow. As a solution, the phase-change detection considers the existence of a phase change in each cell and thus is applicable for modular heat exchangers with multiple phase transitions. It can detect a finite number of phase transitions according to the number of discretization cells. By using a larger number of discretization cells, the accuracy of the algorithm is improved.

4.2. Model verification

To verify and show the two-phase model capabilities, three consecutive steps in the exhaust gas heat flow rate are simulated. The normalized inlet exhaust gas temperature is kept constant at $T_{g,in}^* = 1.6$ while the exhaust gas mass flow rate is varied stepwise from $\dot{m}_g^* = 0.6$ to $\dot{m}_g^* = 0.7$ and finally to $\dot{m}_g^* = 0.34$. This corresponds to 55 kW, 65 kW and 32 kW, respectively, thermal power available on the exhaust gas side. The initial condition of the wall and working fluid temperature is chosen equal to the ambient temperature of 22°C. The boundary condition for the working fluid side is chosen to be constant: normalized working fluid mass flow $\dot{m}_f^* = 0.5$, inlet normalized working fluid temperature $T_{f,in}^* = 0.6$, and normalized working fluid pressure $p_f^* = 0.4$. The working fluid boundary condition is chosen such that vapor is obtained at the heat exchanger outlet for the first 55 kW exhaust gas heat flow rate to show a heat-up simulation from ambient condition.

Fig. 6 shows the outlet working fluid and exhaust gas temperature evolution and the vapor ratio of the working fluid. As expected, the working fluid runs through all three regions, liquid, two-phase and vapor, during the heat-up phase (0–100 s). Then, between 200 and 400 s, the working fluid temperature reaches a new steady-state value, in the super-heated region, due to an increased exhaust gas heat flow rate. At 400 s, the step applied in the exhaust gas heat flow rate is no longer sufficient to generate vapor at the heat exchanger outlet. Thus, the working fluid goes into the two-phase region where the working fluid temperature is constant and equal to the saturation temperature (see Fig. 6).

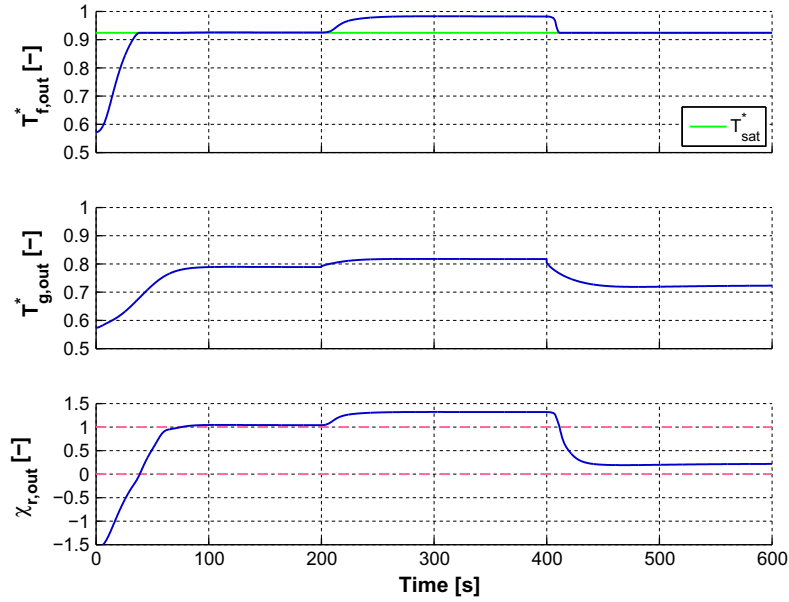


Fig. 6. Normalized outlet working fluid temperature, exhaust gas temperature and working fluid vapor ratio during three consecutive steps in the exhaust gas heat flow rate.

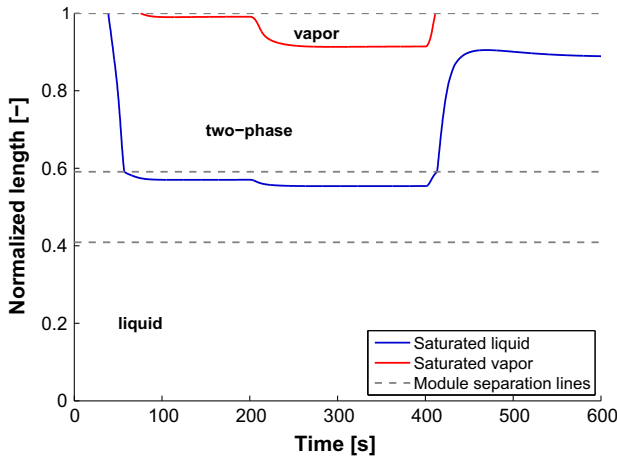


Fig. 7. Normalized liquid and vapor boundaries.

This is also indicated by the vapor ratio χ_r between 0 and 1 at the heat exchanger outlet.

In Fig. 7 the saturated liquid and saturated vapor boundaries inside the evaporators are given. These boundaries are in correspondence with the vapor ratio (see Fig. 6): when $\chi_r \leq 0$, no boundary is present; when $0 < \chi_r < 1$, only the liquid boundary is present; and in case $\chi_r \geq 1$, both boundaries are present. Furthermore, due to the heat exchanger modular design, the boundaries appear to be non-smooth when passing from one module to another. The effect is expected since the heat flux from the exhaust gas to the working fluid differs for each module.

In Fig. 8, the heat flow rate on both the working fluid side and exhaust gas side including losses are shown. As expected, the exhaust gas heat flow rate including losses, equals the working fluid heat flow rate as the system reaches steady state. Furthermore, the mass balance on the working fluid side is shown to be satisfied. On top of that, for transients conditions the outlet working fluid mass flow increases during heating and decreases during cooling.

The next section is dedicated to the experimental validation of the EGR heat exchanger model.

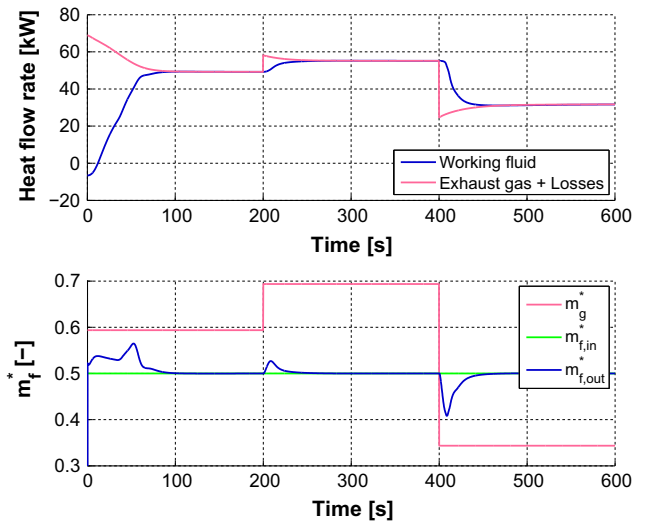


Fig. 8. Heat flow rate and normalized mass balance.

5. Experimental validation

In this section, we verify the overall energy balance for the measurements, followed by the heat exchanger model validation. The energy balance is necessary to verify the measurements correctness. For stationary conditions, the energy equations are:

$$\dot{Q}_g = \dot{m}_g c_{pg} (T_{g,in} - T_{g,out}), \quad (23a)$$

$$\dot{Q}_f = \dot{m}_f (h_{f,out} - h_{f,in}). \quad (23b)$$

In the ideal case where no losses are present $\dot{Q}_g = \dot{Q}_f$ in steady-state. A disagreement between \dot{Q}_g and \dot{Q}_f is an indicator for heat losses or for possible errors in the measurement system. From (4), the calculated heat losses $\dot{Q}_{loss,ss}$ appear to be small, between 100 and 400 W as a consequence of the good heat exchanger insulation. However, from the measurements, see Fig. 9, the energy imbalance between \dot{Q}_g and \dot{Q}_f is more significant, up to 6 kW. This requires closer analysis since it can induce a large error between the measured temperatures and the model prediction.

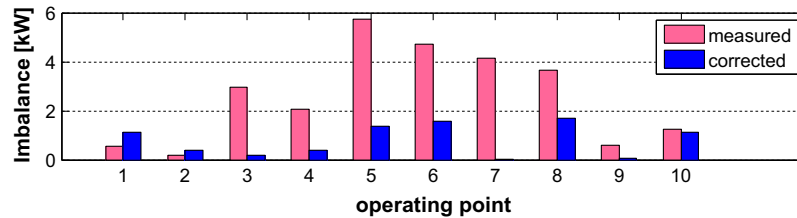


Fig. 9. Energy imbalance for different operating conditions.

In steady-state, the energy imbalance observed for the experiments can be due to several factors: inaccuracies in exhaust gas and working fluid properties and measurement errors. The exhaust gas properties are related to the heat capacity, which is considered to be constant in (23), but the exhaust gas heat capacity varies with temperature. However, within the temperature window that the system operates only 2% error in the computed energy is induced by taking a constant heat capacity. Furthermore, the working fluid property equations used to compute the enthalpy are not exact but approximate the working fluid used within the experimental set-up. The above reasons did not explain the imbalance. Further investigations revealed that the energy imbalance was mainly due to mass flow measurement errors. The mass flow sensors, on the working fluid and exhaust side, were determined to have large systematic error for high mass flow rates that correspond to a high heat flow rate. This is mainly caused by the pulsating flow as a consequence of the pumping behavior on both the working fluid side and engine side. To account for these effects, data reconciliation techniques [29] can be used. These techniques consider the correction of the measured values, such as mass flow rate, by minimizing a least-square error objective function subject to the energy conservation principles (23). The resulting mass flow correction for the exhaust gas side and working fluid side are:

$$\dot{m}_g^c = c_1 \dot{m}_g + c_2, \quad \dot{m}_f^c = c_3 \dot{m}_f + c_4, \quad (24)$$

where c_1 , c_3 are the gain and c_2 , c_4 are the offset mass flow corrections, respectively. Fig. 9 shows that the mass flow corrections lead to an improved energy balance. Using these corrections, the remaining maximum error reduces to 2 kW.

Note that the problem considered is dynamic, while the mass flow corrections, (24), based on an energy balance, (23), are in steady-state. Certainly, also the mass flow sensor dynamic response is important for accurate measurements. However, a direct assessment of the sensor dynamics was not possible. Indirectly it follows from calibration, that this was not a significant effect. Moreover, based on the simulation results, we show that using (24) produces acceptable results also during transients.

The model validation is performed using measured data from a Euro VI heavy-duty diesel engine. Note that different data sets are used for energy balance correction and for the model validation. The data sets used for model validation cover the complete engine operating condition. The first data set consists of several operating points obtained by changing the engine load step-wise. The second data set is a World Harmonized Transient Cycle (WHTC) [30], used to validate the model for normal driving, during cold-start and hot-start conditions. The focus is on verifying the model accuracy regarding the working fluid temperature, vapor ratio and exhaust gas temperature and on confirming that objectives (i)–(iii) are fulfilled.

In Fig. 10, input signals of the first data set are shown. These were recorded by running the engine, with standard Euro-VI calibration, in different operating conditions over the engine speed range of 1200–1850 rpm and engine torque range of 500–2600 Nm.

Initially, the engine is warm and vapor is generated at the heat exchanger outlet. The simulation results in comparison with experimental data are given in Fig. 11. The working fluid, exhaust gas outlet temperatures, and vapor ratio describe well the measurements over the complete operating range. Since the instrumentation to measure the vapor ratio χ_r was not available, the vapor ratio is calculated based on the working fluid temperature and pressure measurements. However, this calculation can be performed only in the liquid region and vapor region, where the working fluid temperature is not saturated. Therefore, a comparison in the two-phase region is not possible.

At 6200 s (see Fig. 11), an increase in the working fluid and exhaust gas temperature is present. This increase in both temperatures is caused by a rapid descend in working fluid mass flow during an increase in the exhaust gas mass flow from the engine (see Fig. 10).

The prediction errors are computed as follows. Let the temperature from simulation and measurement in Kelvin be T_{sim} and T_{meas} , respectively. The error in percentage for both the working fluid side and exhaust side is defined as:

$$e = 100 \cdot \frac{|T_{sim} - T_{meas}|}{|T_{in} - T_{out}|_{max}}, \quad (25)$$

where $|T_{sim} - T_{meas}|$ is the absolute error and $|T_{in} - T_{out}|_{max}$ is the temperature difference over the heat exchanger at maximum thermal load. For the working fluid side, the temperature difference at maximum thermal load corresponds to 215 K, and for the exhaust gas side to 450 K, respectively. Note that (25) is still valid in case normalized temperature values (11) are used.

The mean absolute error for steady-state conditions is 6 K for the working fluid side and 3 K for the exhaust gas side. This corresponds to 2.8% and 0.7% relative error on the working fluid side and exhaust gas side, respectively. The maximum deviation in steady-state is 23 K for the working fluid side and 12 K for the exhaust gas side, corresponding to 10.7% and 2.7%, respectively. Primarily, this is a consequence of the uncertainties in the measurements, which still results in an energy imbalance of up to 2 kW. For low heat flows, the energy imbalance represents approximately 10% of the energy up-take from the exhaust gas. As a consequence, the temperature prediction can be worse for low heat flow rates. For instance in case of a 20 kW transferred heat with an energy imbalance of 2 kW on the working fluid side, results in a working fluid temperature prediction error of approximately 45 K.

The modeling uncertainties, for instance the working fluid properties and heat transfer coefficient, also play a role for model accuracy. As can be seen between 6000–8000 s and 12,000–14,000 s, that a slightly higher heat transfer coefficient would improve the results. From a dynamical point of view, incorporating conduction in the casing, especially between modules, might improve the model accuracy during transients. Thus, using a more accurate measurement system, heat transfer coefficient for plates instead of tubes and conduction in the casing, can lead to more accurate results. The error induced due to numerical approximation is small compared to the error due to modeling uncertainties.

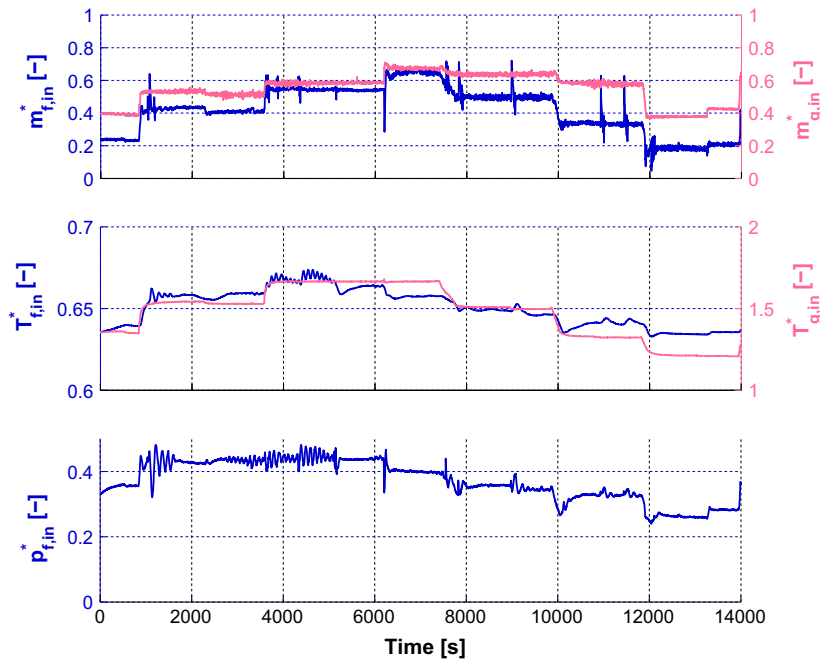


Fig. 10. Experimental input signals.

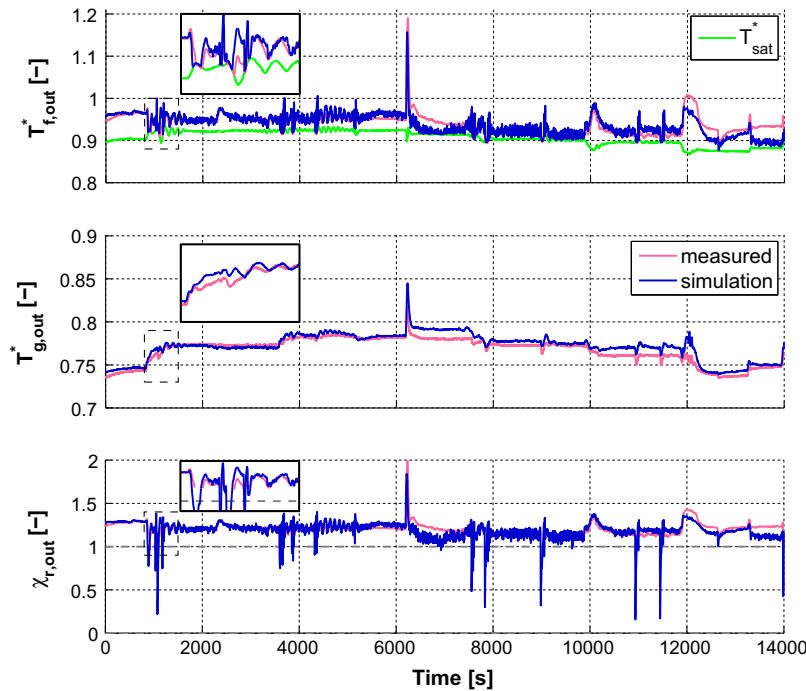


Fig. 11. Working fluid temperature, exhaust gas temperature and vapor ratio in comparison with measurements.

Reducing the sample time and increasing the number of cells does not significantly improve the results.

To validate the model for representative real-world driving conditions, we use a standard WHTC during cold-start and hot-start. The WHTC type approval cycle is a transient test of 1800 s that covers typical driving conditions: urban, rural and highway. This cycle generates in terms of mass flows, temperatures and pressure the input data shown in Fig. 12a and in Fig. 12b during cold-start and hot-start, respectively. On the exhaust gas side, the mass flow responds almost immediately, while the temperature has a first

order behavior with a time constant of approximately 16 s. Furthermore, on the working fluid side, slower dynamic behavior can be seen for the mass flow rate, temperature and pressure in the system.

The simulation results for the cold-start and hot-start WHTC are given in Fig. 13a and in Fig. 13b, respectively. Note that the instrumentation to measure the vapor ratio χ_r was not available. In the liquid and vapor region, the vapor ratio χ_r is calculated from (10) based on measured working fluid temperature and pressure. In the two-phase region, the measured temperature equals the

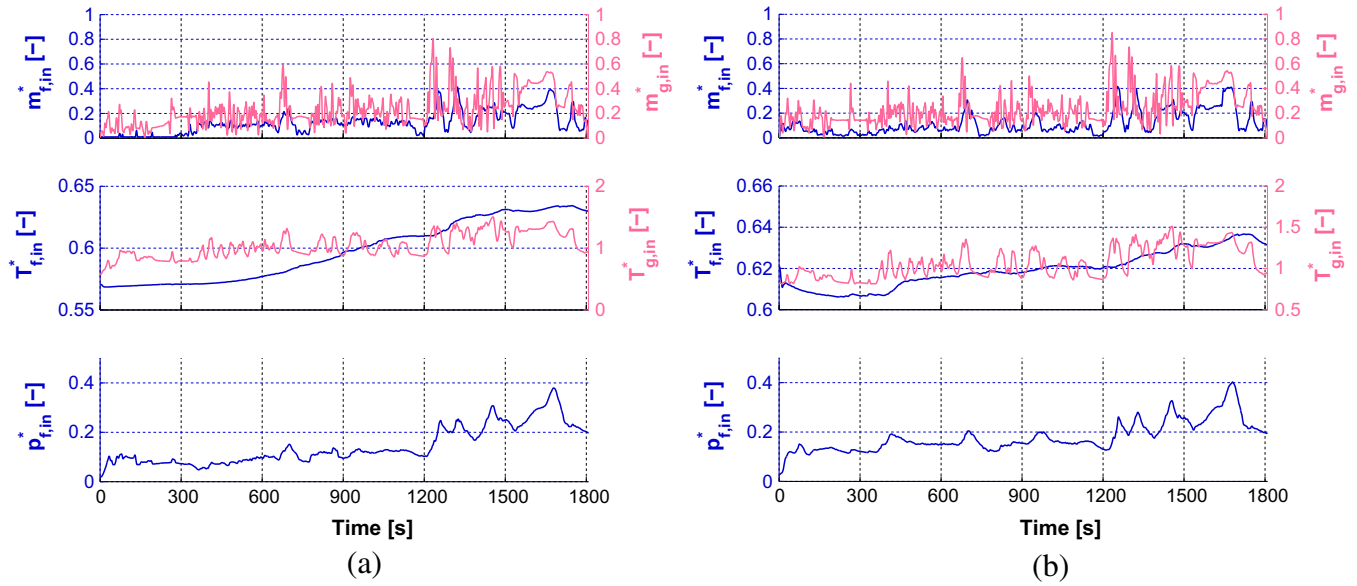


Fig. 12. (a) Experimental input signals from a cold-start WHTC. (b) Experimental input signals from a hot-start WHTC.

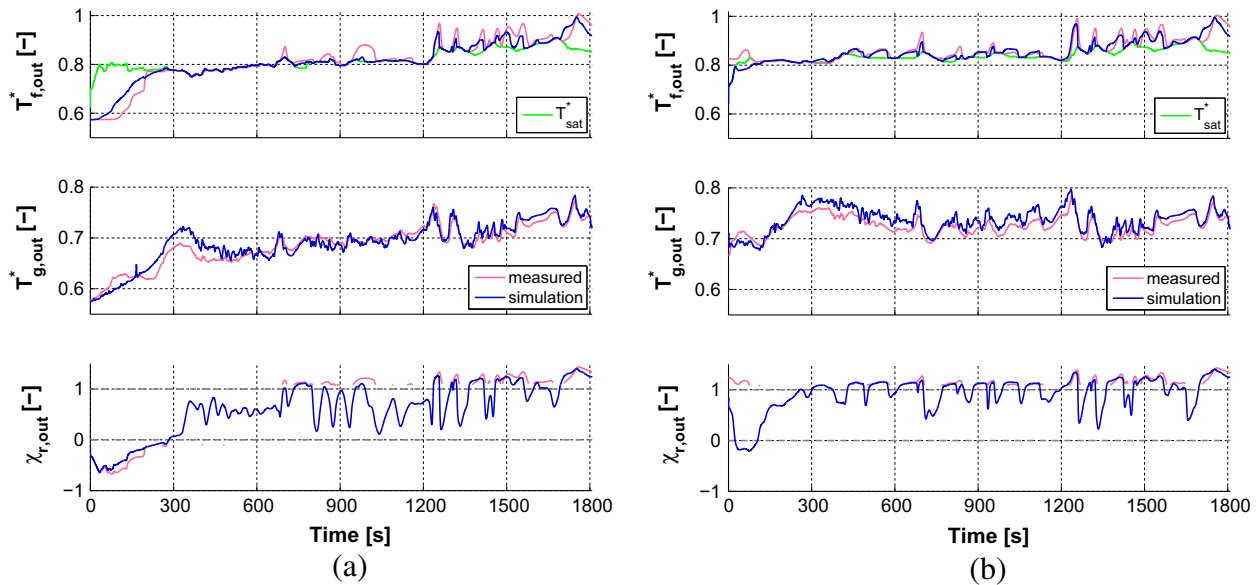


Fig. 13. (a) Normalized working fluid temperature, exhaust gas temperature and vapor ratio for the cold-start WHTC. (b) Normalized working fluid temperature, exhaust gas temperature for the hot-start WHTC.

saturation temperature, while having no information about the vapor ratio. Thus, a direct comparison of the vapor ratio with respect to the measurements is not possible. However, using a highly dynamic test cycle, the working fluid at the heat exchanger outlet switches between the two-phase and the vapor region repeatedly. From the simulation results, the moment of switching between these two regions is well described (see Fig. 13). This is important for a control strategy that needs to guarantee safe system operation.

For the cold-start WHTC the ambient initial condition is used. First, regarding the fast dynamic capabilities during normal operating conditions, namely after 1200 s within the WHTC, the model gives good results with respect to the measurements. Dynamic behavior of the working fluid temperature, exhaust gas tempera-

ture and vapor ratio are well captured. Second, the model shows that during the heating-up process, between 200 and 400 s, the working fluid temperature rises more rapidly in comparison with the measurement. As a consequence of the energy conservation principle, also the exhaust gas temperature shows a slight disagreement with the measurements. This effect is mainly caused by the casing material for which a simple first order model was used. The result can therefore be improved, by including a more accurate heat loss model for the casing. However, for a long haul application, the start-up appears for a very limited time, typically only 6–7 min (see Fig. 13a), compared to the complete operation time, which is in the order of hours. In practice, the start-up can be accommodated in the controller design using for instance a start-up procedure to bring the system from a cold condition to a

state close to the desired operating condition. Another controller that is designed for normal operating conditions can be activated from that point.

For the hot-start WHTC, in terms of accuracy, the results are similar to the cold-start WHTC. Note however, that the model initial condition is challenging to choose, since the system is not in steady-state and the current state for the real system is unknown. This results in a less accurate solution for the first 100 s (see Fig. 13b). In contrast with a non-modular heat exchanger, where the liquid and vapor boundaries appear once as a function of time, in a modular heat exchanger multiple phase transitions can be present. Fig. 14 shows the model capabilities to capture multiple phase transitions in single flow. Between 100 and 300 s, is the most prominent time interval where multiple liquid to two-phase transitions are encountered. Similarly, multiple two-phase to vapor transitions can be present, however, they are less visible due to high fluid velocities. In general, these transitions appear during transients and vanish as the system reaches its steady-state value.

For highly dynamic conditions, the model describes the real system well: working fluid temperature error is below 40 K with vapor ratio well captured and exhaust gas temperature error is below 20 K for the complete operating range. This result is obtained despite the accuracy of the experimental data that can lead to working fluid temperature errors up to 45 K. Thus, the model complies with the proposed objectives (i)–(iii), for WHR system safe operation, control design and emission management, respectively.

In Table 2, the maximum and average model prediction error is summarized for steady state and dynamic conditions.

Regarding computational complexity, the model computational time is approximately 300 times less as compared to the measurements time length. The results were obtained by running the discrete heat exchanger model with 22 cells and a sampling time of 0.2 s on a Lenovo laptop with Windows 7, Matlab 2012a and 2 GHz quad-core processor. The simulation results show that overall a good agreement between the model and experiments is obtained while computational complexity is low.

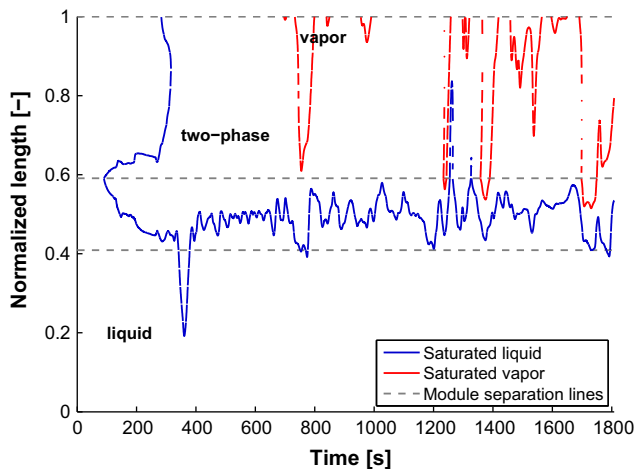


Fig. 14. Normalized liquid and vapor boundaries for WHTC cold-start.

Table 2
Summary of the model prediction error.

	Working fluid		Exhaust gas	
	Maximum	Average	Maximum	Average
Steady state	23 K (10.7%)	6 K (2.8%)	12 K (2.7%)	3 K (0.7%)
Dynamic	37 K (17.2%)	8 K (3.7%)	19 K (4.2%)	5 K (1.1%)

6. Conclusions

A dynamic model of a modular two-phase heat exchanger for waste heat recovery in diesel engines was developed. The studied waste heat recovery system recovers energy from both the exhaust gas recirculation line and main exhaust line. In this study, the modular heat exchanger was described in detail based on the mass and energy balance equations. The model was brought into a non-dimensional form to reduce the number of free parameters while avoiding numerical difficulties. The resulting representation was discretized in time and space using a finite difference and a staggered grid approach. Compared to other heat exchanger models, the model developed in this paper combines the finite difference method with the moving boundary modeling approach. Thus, it captures the dynamics of multiple phase transition caused by the modular heat exchanger design. The model was validated on data from a state-of-the-art Euro-VI heavy-duty diesel engine equipped with a waste heat recovery system. The validation was performed on two data sets: transitions between steady-state points that cover the complete engine operating area and a highly dynamic world harmonized transient cycle for both cold-start and hot-start conditions. From the simulation results, it is concluded that the model is a good representation of the real system capable to predict the working fluid and exhaust gas temperature with an average error of less than 4%.

The model developed in this paper will be first included in a complete waste heat recovery system model. The complete model will be used to develop low-level control strategies that optimize the waste heat recovery system power output within safe operation limits. Second, the supervisory control strategy [31] will be further developed and implemented on the studied engine.

Acknowledgements

The research presented in this paper is financially supported by TNO Automotive, The Netherlands. The authors are grateful to Frank Kupper, Xander Seykens and Chepa Rojer for valuable comments and discussions.

Appendix A. Working fluid properties

The normalized saturation temperature as a function of normalized pressure is shown in Fig. A.1. The saturation temperature is the temperature for a corresponding pressure at which a liquid boils into its vapor phase. A mathematical relation to describe the saturation temperature is given in [32]:

$$T_{sat}^* = \frac{1}{T_c} \left(\frac{b_s}{a_s - (\log_{10} p_f - 5)} - c_s \right), \quad (A.1)$$

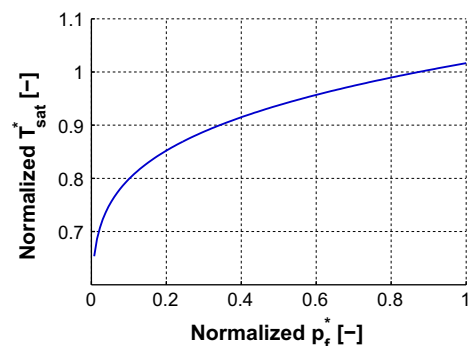


Fig. A.1. Normalized working fluid saturation temperature as a function of pressure.

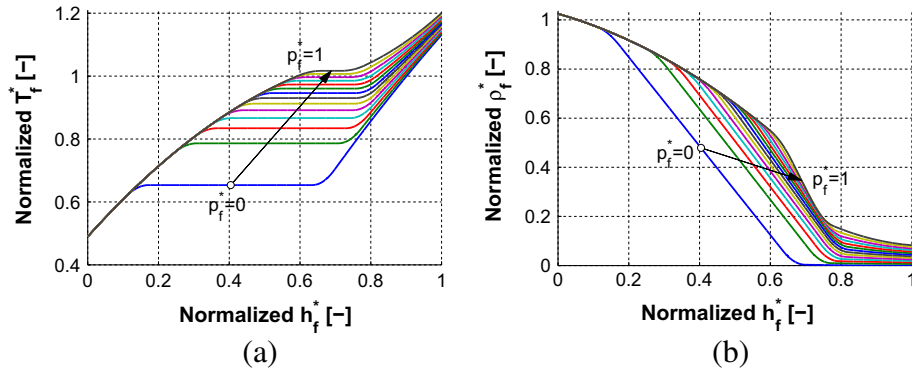


Fig. A.2. (a) Normalized working fluid temperature as a function of specific enthalpy and pressure. (b) Normalized working fluid density as a function of specific enthalpy and pressure.

where p_f is the working fluid pressure. For ethanol the constants a_s , b_s and c_s are taken from [32].

In Fig. A.2a the normalized temperature-enthalpy characteristic of the working fluid for different values of the pressure is presented. The working fluid temperature can be approximated as follows:

$$T_f^* = \begin{cases} a_l h_f^{*2} + b_l h_f^* + c_l & \text{if } h_f^* \leq h_{l1}^* \\ a_{sl} h_f^{*3} + b_{sl} h_f^{*2} + c_{sl} h_f^* + d_{sl} & \text{if } h_{l1}^* < h_f^* < h_{l2}^* \\ T_{sat}^* & \text{if } h_{l2}^* \leq h_f^* \leq h_{v1}^* \\ a_{sv} h_f^{*3} + b_{sv} h_f^{*2} + c_{sv} h_f^* + d_{sv} & \text{if } h_{v1}^* < h_f^* < h_{v2}^* \\ a_v h_f^{*2} + b_v h_f^* + c_v & \text{if } h_f^* \geq h_{v2}^* \end{cases}, \quad (\text{A.2})$$

where a_l , b_l , c_l are constants used for the temperature-enthalpy characteristic on the liquid region. In the two-phase region the normalized working fluid temperature is constant and equal to the normalized saturation temperature T_{sat}^* . The vapor region is approximated using pressure dependent coefficients:

$$a_v = a_{v1} p_f^* + a_{v0}, \quad b_v = b_{v1} p_f^* + b_{v0}, \quad c_v = c_{v1} p_f^* + c_{v0}. \quad (\text{A.3})$$

Let us define the normalized saturated liquid enthalpy h_{l1}^* and vapor enthalpy h_{v1}^* as a function of T_{sat}^* :

$$h_{l1}^* = \frac{-b_l + \sqrt{b_l^2 - 4a_l(c_l - T_{sat}^*)}}{2a_l}, \quad (\text{A.4a})$$

$$h_{v1}^* = \frac{-b_v + \sqrt{b_v^2 - 4a_v(c_v - T_{sat}^*)}}{2a_v}. \quad (\text{A.4b})$$

In (A.2), two cubic functions are introduced to impose a smooth transition from liquid to two-phase and from two-phase to vapor. The coefficients of these cubic functions are obtained by solving a set of four linear equations at a specified normalized pressure p_f^* . The four linear equations follow by enforcing continuity and imposing the same slope at each of the chosen thresholds h_{l1}^* and h_{l2}^* . Around the liquid and vapor saturation point, a similar procedure is employed.

The thresholds used in (A.2) are defined as:

$$\begin{aligned} h_{l1}^* &= h_l^* - \Delta h^*, & h_{l2}^* &= h_l^* + \Delta h^*, \\ h_{v1}^* &= h_v^* - \Delta h^*, & h_{v2}^* &= h_v^* + \Delta h^*, \end{aligned} \quad (\text{A.5})$$

where Δh^* is a positive value, upper limited by the critical pressure such that h_{l2}^* does not become larger than h_{v1}^* .

In Fig. A.2b the normalized working fluid density as a function of enthalpy and pressure is illustrated. The expression which describes the density is

$$\rho_f^* = \begin{cases} a_{\rho l} h_f^{*2} + b_{\rho l} h_f^* + c_{\rho l} & \text{if } h_f^* \leq h_{l1}^* \\ a_{\rho sl} h_f^{*3} + b_{\rho sl} h_f^{*2} + c_{\rho sl} h_f^* + d_{\rho sl} & \text{if } h_{l1}^* < h_f^* < h_{l2}^* \\ \frac{\rho_v^* - \rho_l^*}{h_v^* - h_l^*} h_f^* + \frac{h_v^* \rho_l^* - h_l^* \rho_v^*}{h_v^* - h_l^*} & \text{if } h_{l2}^* \leq h_f^* \leq h_{v1}^* \\ a_{\rho sv} h_f^{*3} + b_{\rho sv} h_f^{*2} + c_{\rho sv} h_f^* + d_{\rho sv} & \text{if } h_{v1}^* < h_f^* < h_{v2}^* \\ a_{\rho v} h_f^{*2} + b_{\rho v} h_f^* + c_{\rho v} & \text{if } h_f^* \geq h_{v2}^* \end{cases} \quad (\text{A.6})$$

where $a_{\rho l}$, $b_{\rho l}$, $c_{\rho l}$ are constants used to approximate the density-enthalpy characteristic for the liquid region. In the vapor region the polynomial coefficients are quadratic expressions of the form

$$a_{\rho v} = a_{\rho v2} p_f^{*2} + a_{\rho v1} p_f^* + a_{\rho v0}, \quad (\text{A.7a})$$

$$b_{\rho v} = b_{\rho v2} p_f^{*2} + b_{\rho v1} p_f^* + b_{\rho v0}, \quad (\text{A.7b})$$

$$c_{\rho v} = c_{\rho v2} p_f^{*2} + c_{\rho v1} p_f^* + c_{\rho v0}, \quad (\text{A.7c})$$

since linear expressions are too weak approximations of the real characteristic given in Fig. A.2b. The saturated liquid and vapor density are given by

$$\rho_l^* = a_{\rho l1} h_{l1}^{*2} + b_{\rho l1} h_{l1}^* + c_{\rho l1}, \quad (\text{A.8a})$$

$$\rho_v^* = a_{\rho v1} h_{v1}^{*2} + b_{\rho v1} h_{v1}^* + c_{\rho v1}. \quad (\text{A.8b})$$

As for the temperature-enthalpy characteristic also for the density-enthalpy characteristic a set of four linear equations are solved to find the cubic function coefficients. The reason for smoothing the working fluid properties is to avoid discontinuities in the working fluid enthalpy derivative around the liquid and vapor saturation curves, which can cause the phenomenon of chattering. Due to this phenomenon, the computed variables can exceed acceptable boundaries, causing simulation failures.

References

- [1] Charles S, Christopher D. Review of organic Rankine cycles for internal combustion engine exhaust waste heat recovery. *Appl Therm Eng* 2013;51(1–2):711–22.
- [2] Endo T, Kawajiri S, Kojima Y, Takahashi K, Baba T, Ibaraki S, et al. Study on maximizing exergy in automotive engines. In: SAE international, Detroit, Michigan. SAE paper: 2007-01-0257; 2007.
- [3] Hounsham S, Stobart R, Cooke A, Childs P. Energy recovery systems for engines. In: SAE international, Detroit, Michigan. SAE paper: 2008-01-0309; 2008.
- [4] Schuster A, Karellas S, Aumann R. Efficiency optimization potential in supercritical organic Rankine cycles. *Energy* 2010;35(2):1033–9.
- [5] Gao W, Zhai J, Li G, Bian Q, Feng L. Performance evaluation and experiment system for waste heat recovery of diesel engine. *Energy* 2013;55:226–35.
- [6] Hountalas D, Katsanos C, Kouremenos D, Rogdakis E. Study of available exhaust gas heat recovery technologies for HD diesel engine applications. *Int J Altern Propul* 2007;1(2):228–49.
- [7] Weerasinghe W, Stobart R, Hounsham S. Thermal efficiency improvement in high output diesel engines a comparison of Rankine cycle with turbo-compounding. *Appl Therm Eng* 2010;30(14–15):2253–6.

- [8] Xiaolong G, Suwen Y, Heng X, Qiang O. A dynamic model for thermoelectric generator applied in waste heat recovery. *Energy* 2013;52:201–9.
- [9] Badami M, Mura M. Preliminary design and controlling strategies of a small-scale wood waste Rankine cycle (RC) with reciprocating steam engine (SE). *Energy* 2009;34(9):1315–24.
- [10] Dolz V, Novella R, Garcia A, Sanchez J. HD diesel engine equipped with a bottoming Rankine cycle as a waste heat recovery system. Part 1: Study and analysis of the waste heat energy. *Appl Therm Eng* 2012;36:269–78.
- [11] Katsanos C, Hountalas D, Pariotis E. Thermodynamic analysis of a Rankine cycle applied on a diesel truck engine using steam and organic medium. *Energy Convers Manage* 2012;60:68–76.
- [12] Ziviani D, Beyene A, Venturini M. Advances and challenges in ORC systems modeling for low grade thermal energy recovery. *Appl Energy* 2014;121:79–95.
- [13] Willatzen M, Pettit N, Ploug-Sorensen L. A general dynamic simulation model for evaporators and condensers in refrigeration. Part I–II. *Int J Refrig* 1998;21(5):398–414.
- [14] Wei D, Lu X, Lu Z, Gu J. Dynamic modeling and simulation of an organic Rankine cycle (ORC) system for waste heat recovery. *Appl Therm Eng* 2008;28(10):1216–24.
- [15] Zhang J, Zhang W, Guolian H, Fang F. Dynamic modeling and multivariable control of organic Rankine cycles in waste heat utilizing processes. *Comput Math Appl* 2012;64:908–21.
- [16] McKinley T, Alleyne G. An advanced nonlinear switched heat exchanger model for vapor compression cycles using the moving-boundary method. *Int J Refrig* 2008;31(7):1253–64.
- [17] MacArthur J, Gald E. Unsteady compressible two-phase flow model for predicting cyclic heat pump performance and a comparison with experimental data. *Int J Refrig* 1989;12:29–41.
- [18] Jensen JM. Dynamic modeling of thermo-fluid systems. Ph.D. Thesis, Technical University of Denmark; 2003.
- [19] Quoilin S, Aumann R, Grill A, Schuster A, Lemort V, Spliethoff H. Dynamic modeling and optimal control strategy of waste heat recovery organic Rankine cycles. *Appl Energy* 2011;88(6):2183–90.
- [20] Mandrusiak G, Carey V. A finite difference computational model of annular film-flow boiling and two-phase flow in vertical channels with offset strip fins. *Int J Multiphase Flow* 1990;16(6):1071–96.
- [21] Lo Brano V, Ciulla G, Piacentino A, Cardona F. Finite difference thermal model of a latent heat storage system coupled with a photovoltaic device: description and experimental validation. *Renew Energy* 2014;68:181–93.
- [22] Horst T, Rottengruber H, Seifert M, Ringler J. Dynamic heat exchanger model for performance prediction and control system design of automotive waste heat recovery systems. *Appl Energy* 2013;105:293–303.
- [23] Feru E, Willems F, Rojer C, de Jager B, Steinbuch M. Heat exchanger modeling and identification for control of waste heat recovery systems in diesel engines. In: *Proceedings of the American control conference*, Washington DC, USA; 2013, p. 2860–5.
- [24] Feru E, Kupper F, Rojer C, Seykens X, Scappin F, Willems F, et al. Experimental validation of a dynamic waste heat recovery system model for control purposes. In: *SAE international*, Detroit, Michigan. SAE paper: 2013-01-1647; 2013.
- [25] Pham MV, Plourde F, Doan SK. Large-eddy simulations of staggered parallel-plate fin heat exchangers: effect of Reynolds number on flow topology. *Numer Heat Transfer, Part A: Appl* 2008;53(4):354–76.
- [26] VDI-Gesellschaft Verfahrenstechnik und Chemieingenieurwesen. *VDI Heat Atlas*, Springer, Berlin, Germany; 2010.
- [27] Thome John R. *Engineering data book III*. Lausanne, Switzerland: Wolverine Tube, Inc.; 2010.
- [28] Ziviani D, Beyene A, Venturini M. Universal approach to predicting saturated flow boiling heat transfer in mini/micro-channels Part II. Two-phase heat transfer coefficient. *Int J Heat Mass Transfer* 2013;64:1239–56.
- [29] Bagajewicz MJ, Cabrera E. Data reconciliation in gas pipeline systems. *Ind Eng Chem Res* 2003;42(22):5596–606.
- [30] Heinz S. Development of a worldwide harmonised heavy-duty engine emissions test cycle. Tech. rep. TRANS/WP29/GRPE/2001/2, United Nations; April 2001.
- [31] Willems F, Kupper F, Rascanu G, Feru E. Integrated energy and emission management for diesel engines with waste heat recovery using dynamic models. *Oil Gas Sci Technol Rev IFP Energies Nouv* 2014:1–16.
- [32] Ambrose D, Sprake CHS, Townsend R. Thermodynamic properties of organic oxygen compounds. XXXVII. vapour pressures of methanol, ethanol, Pentan-1-ol, and Octan-1-ol from the normal boiling temperature to the critical temperature. *J Chem Thermodynam* 1975;7(2):185–90.